The Delay Multiply and Sum Beamforming Algorithm in Ultrasound B-Mode Medical Imaging

Giulia Matrone, *Member, IEEE*, Alessandro Stuart Savoia, *Member, IEEE*, Giosuè Caliano, *Senior Member, IEEE*, and Giovanni Magenes, *Member, IEEE*

***Abstract*— Most of ultrasound medical imaging systems currently on the market implement standard Delay and Sum (DAS) beamforming to form B-mode images. However, image resolution and contrast achievable with DAS are limited by the aperture size and by the operating frequency. For this reason, different beamformers have been presented in the literature that are mainly based on adaptive algorithms, which allow achieving higher performance at the cost of an increased computational complexity.**

In this paper we propose the use of an alternative non-linear beamforming algorithm for medical ultrasound imaging, which is called Delay Multiply and Sum (DMAS) and that was originally conceived for a RADAR microwave system for breast cancer detection. We modify the DMAS beamformer and test its performance on both simulated and experimentally collected linear-scan data, by comparing the Point Spread Functions, beampatterns, synthetic phantom and *in vivo* carotid artery images obtained with standard DAS and with the proposed algorithm. Results show that the DMAS beamformer outperforms DAS in both simulated and experimental trials and that the main improvement brought about by this new method is a significantly higher contrast resolution (i.e. narrower main lobe and lower side lobes), which turns out into an increased dynamic range and better quality of B-mode images.

***Index Terms*— Beamforming, contrast resolution, Delay Multiply and Sum, ultrasound medical imaging**

I. Introduction

ULTRASOUND (US) image quality, in terms of resolution and contrast, is deeply affected by the beam properties [1].

The unit in charge of implementing all the techniques to focus and steer the array of transducers in the ultrasound probe towards a desired direction or point in space, while optimizing the beam shape, is called beamformer. The beamformer generates the delay and weight pattern to be applied each time to the array elements during transmission or reception. Thus, an accurate design of this unit is fundamental to improve the beam shape and, consequently, the US imaging system performance, which is especially important in medical diagnostic applications.

The main goal of the beamformer is to generate a beam with low side lobes, over an as long as possible depth, and with a narrow main lobe [2], which unfortunately are two opposing objectives. Actually, the beam main-lobe width determines system resolution, while side-lobe level determines image contrast and affects the dynamic range achievable for image visualization. The beamformer should optimize the beam by operating a good trade-off among all these parameters and, for this reason, it can be considered one of the most important and complex building blocks in the ultrasound system [3].

In medical ultrasound imaging, the standard technique used for image reconstruction is the Delay and Sum (DAS) beamforming algorithm [2], [4], which however shows a limited imaging resolution and reduced off-axis interference rejection.

Other more powerful image formation techniques, traditionally employed in RADAR or SONAR systems, were proposed in the literature for possible application in medical ultrasound beamforming, such as adaptive beamformers, able to dynamically change the receive aperture weights based on the received data statistics [5] and to achieve an increased resolution, but at the cost of a higher computational complexity. These include, for example, methods based on the Capon/Minimum Variance beamformer [6-11], beamformers which use target-dependent coherence-based weighting [12], or a combination of both [13], and adaptive beamformers based on the Constrained Least Mean Squares theory [14]. In [15] an example of a data-independent beamformer employing finite impulse response (FIR) filters on each receive channel, instead of single apodization weights, was described.

In this paper we present an improved version of a beamforming algorithm called Delay Multiply and Sum (DMAS), which was previously introduced by Lim et al. [16] in a study on RADAR imaging applications for the early detection of breast cancer. Similarly to DAS, the DMAS algorithm focuses the received beam by applying

Manuscript received September 24, 2014. This work has been partially supported by the National governments and the European Union through the ENIAC JU project DeNeCoR under grant agreement number 324257.

G. Matrone and G. Magenes are with the Dipartimento di Ingegneria Industriale e dell'Informazione, Università degli Studi di Pavia, 27100 Pavia, Italy (corresponding author e-mail: giulia.matrone@unipv.it).

A. S. Savoia and G. Caliano are with the Dipartimento di Ingegneria, Università degli Studi Roma Tre, 00146 Rome, Italy.

geometrically computed delays to the signals coming from the antennas or, in the ultrasound case, from the transducer array elements in the US probe. In the original algorithm, before summation, signals are combinatorially coupled and multiplied. This operation can be interpreted as the aperture auto-correlation function, which means that, at each time instant, the spatial cross-correlation among all the received signals collected by the active transducers is computed. Thus, DMAS is a non-linear beamforming algorithm.

In the past, other methods in the literature addressed non-linear processing and spatial cross-correlation for beam formation or, more generically, target localization. In particular, to overcome inherent limitations of linear beamformers (i.e. those which linearly combine the received signals), non-linear beamformers were proposed, which transform the input data into a higher dimensionality space by means of a non-linear transformation [17]. In [18], for example, an approach based on Radial Basis Functions was introduced, in which the received signals were processed by a series of non-linear basis functions, whose outputs were then weighted and summed to calculate the beamformed signal. In [19], an adaptive Bayesian beamformer implementation based on a non-linear kernel was proposed, and an orthogonal forward selection using the Fisher ratio was employed to find the optimal solution. Neural networks or support vector machines were used to estimate the weights of non-linear beamformers respectively in [17] and [20]. Moreover, in [21] the non-linear effects introduced by envelope detection in the image formation process were investigated and shown to be not negligible indeed.

The cross-correlation operation is generally computed in time-delay estimation (TDE) techniques. In [22] a unifying method called “accumulated correlation” was developed to combine the TDE principle with beamforming, and map correlation values to space. Non-coherent correlation, calculated on the squared modulus of the signal complex envelopes, was employed in [23] to compute a metrics called “collision index” for object localization.

Recently, on the way paved by works on the analysis of US backscattered signal coherence as [24], a new approach based on the spatial correlation of echo signals has been proposed for US medical imaging application, which is called Short Lag Spatial Coherence (SLSC) imaging [25], [26]. Similarly to DMAS, the signals received by the aperture are coupled, multiplied and summed to compute the SLSC image. However, the aim of SLSC is to generate images of the spatial coherence of the US backscattered echoes and not images of their magnitude, as, on the contrary, B-mode imaging techniques do. In the SLSC image, in fact, regions with different scattering strengths can show the same coherence and thus intensity, as the computed cross-correlation is normalized (i.e., each multiplied couple of signals is divided by the square root of the product of the signal variances) and the influence of echo magnitudes is removed [26].

In this work we concentrate on the effects of the spatial cross-correlation operation on the signals involved in the US beamforming process, both in the time and frequency domain, and from such operation we derive a method for US B-mode image formation. To do so, we introduce several new processing steps in the original DMAS algorithm that will be explained in detail.

What we demonstrate in this paper is that, by applying a modified and improved version of the DMAS beamformer on simulated and experimental data, better performance of the US medical imaging system are obtained, such as higher contrast resolution, object definition and dynamic range.

The paper is organized as follows. In Section II we present and describe in detail the DMAS method applied to ultrasound image formation. Then, we compare the DMAS and DAS algorithms both on simulated and on experimentally acquired *in vivo* data, and in Section III we show that better image quality can be achieved with the proposed DMAS beamformer. We discuss and comment the obtained results in Section IV. Finally, the conclusions and some hints for future developments are reported in Section V.

II. Materials and Methods

In order to generate a B-mode ultrasound image with a linear array, for each scan line the active aperture is shifted and the aperture elements focus the beam at a point along the scan path. After each transmission, the back-scattered signals are collected by the transducers in the receive aperture, which convert them into voltage signals that are finally beamformed.

Usually, in a simple DAS beamformer the received signals are delayed (re-aligned) and summed to generate the final output corresponding to the considered scan line. In this way the beamformer aims to re-phase and reinforce those signal components coming from the desired point, while rejecting as much as possible the unwanted interferences coming from other directions.

After the whole scan is completed, the beamformed signals undergo envelope detection, logarithmic compression and further possible signal processing, and finally they are used to form and display the 2D image, which is called scan conversion.

A. Delay Multiply and Sum Beamforming

The DMAS algorithm [16] is schematically illustrated in the block diagram of Fig. 1.

If we consider a single scan line, after beam transmission each transducer in the receive aperture receives a different echo signal, which has travelled along a different path. The first step of the algorithm consists in time-shifting the received RF signals to re-align them as in DAS. Once signals are in phase, they are combinatorially coupled and multiplied: if the number of receive channels is N, then the number of multiplications to be performed is given by all the possible signal pair combinations, that is:

$$\binom{N}{2} = \frac{N^2 - N}{2}, \tag{1}$$

and the DMAS-beamformed signal is obtained as:

$$y_{DMAS}(t) = \sum_{i=1}^{N-1} \sum_{j=i+1}^{N} s_i(t) s_j(t), \tag{2}$$

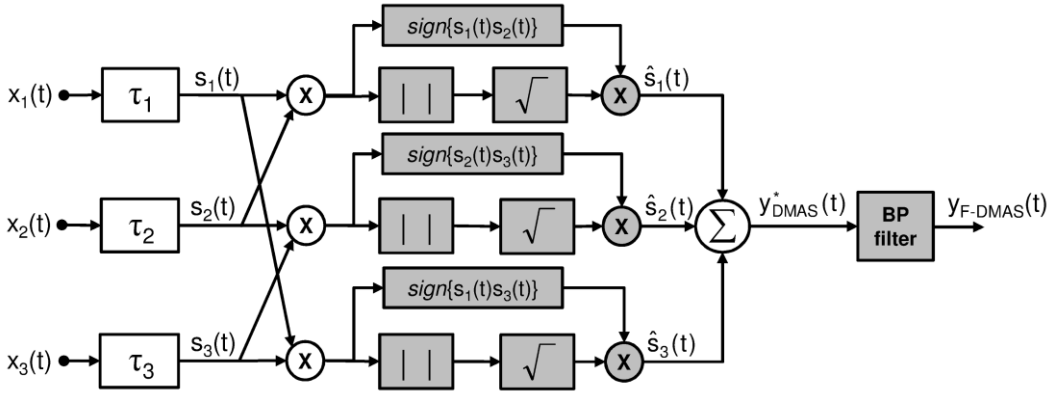

Fig. 1. Improved DMAS beamformer block-diagram. White-background blocks enclose the original DMAS processing steps, while the gray ones refer to the steps introduced in the new version of the algorithm implemented in this work (called F-DMAS). In the figure, a 3-element receive aperture is assumed and x_i (i=1,2,3) are the received RF signals for one scan line. The signals x_i are delayed, coupled and multiplied; then the square root is applied to the absolute values of the multiplied couples while preserving their sign, and the resulting signals are summed and band-pass (BP) filtered. The output $y_{F\text{-}DMAS}$ is used to form the considered image line by demodulation, normalization and log-compression (not shown).

where s_i is the delayed RF voltage signal received by the i-th transducer and y_{DMAS} is the DMAS-beamformed output.

This operation can be mathematically interpreted as the auto-correlation function of the receive aperture, in which, however, the auto-product terms (i=j) are excluded and the coefficients are halved (it does not consider both the s_is_j and s_js_i terms in the summation). In the practice, if the aperture is not apodized (i.e. it is simply weighted by a rectangular window of amplitude 1), its auto-correlation is a triangle-shaped, *2N-1* coefficient function, in which the central vertex amplitude is set to 0. The correlation is not normalized so as to preserve the information on the scatterer relative strengths.

The obtained signal y_{DMAS} cannot be used as is to form the scan line of a conventional B-mode image: due to the multiplication stage, in fact, it is a dimensionally squared (i.e. [Volt^2] instead of [Volt]), partially rectified non-zero mean signal, and therefore envelope detection cannot be applied.

Consequently, in this work we propose to introduce some further processing steps into the original DMAS (gray blocks in Fig. 1), in order to develop a beamforming algorithm for B-mode image formation.

First of all, we derive a new "equivalent RF-signal" by applying the "signed" square root to each s_is_j couple inside the summations (in practical terms, we compute a signed geometrical mean of s_i and s_j), so that the amplitude of each multiplication term is correctly scaled to have the same dimensionality of the RF signals s_i, without losing its sign:

$$\hat{s}_{ij}(t) = sign(s_i(t)s_j(t)) \cdot \sqrt{\left|s_i(t)s_j(t)\right|}. \qquad (3)$$

Thus, if we use n to index all the combinatory couplings of i and j, each new beamformed signal y^*_{DMAS} is computed as:

$$y^*_{DMAS}(t) = \sum_{i=1}^{N-1}\sum_{j=i+1}^{N} \hat{s}_{ij}(t) = \sum_{n=1}^{(N^2-N)/2} \hat{s}_n(t). \qquad (4)$$

Moreover, while the output of DAS beamforming is a zero-mean signal that shows an amplitude spectrum similar to that of the RF signals s_i, both a DC and second harmonic component appear in the spectrum of the DMAS beamformed output. This is due to the fact that, by multiplying the RF signals which have an almost similar frequency content (e.g. a band centered at f_0), two new components generate in the amplitude spectrum of the output signal, i.e. one centered in f_0-f_0=*0* and one in f_0+f_0=$2f_0$. Thus, a further step is introduced in the DMAS processing chain (now called Filtered-DMAS, i.e. F-DMAS) where the beamformed signals y^*_{DMAS} are band-pass (BP) filtered in order to attenuate the DC and higher frequency components, while keeping the one centered on $2f_0$ almost unaltered. Finally, $y_{F\text{-}DMAS}$ is obtained (Fig. 1).

Envelope detection is in the end performed by means of the Hilbert transform and the obtained lines are normalized and log-compressed to form the final image.

All considered, we can expect the F-DMAS technique to bring about the following advantages compared to DAS:

1) the image lateral resolution will be improved, as both the wavelength and f-number (F#) decrease. In particular, the wavelength is halved with respect to DAS, as the F-DMAS beamformed signal spectrum is centered at $2f_0$. At the same time, the number of elements in the new "artificial" aperture is increased, as the auto-correlation function has *2N-1* coefficients, and consequently F# is lowered. On the other hand, the image axial resolution will be unaltered, as the central frequency is doubled but, at the same time, the fractional bandwidth is halved;
2) better clutter and noise rejection will be achieved thanks to the correlation operation, which brings a measure of the backscattered signal coherence into the beamforming process: the output of each multiplication operation is indeed emphasized when the inputs are both high, or it becomes very low when the inputs are both low, and the contribution of outlier uncorrelated samples (which can be due to noise or unwanted interferences) is significantly lowered. Moreover, many more signals are summed together to compute the final output if compared to simple DAS, i.e. $(N^2–N)/2$ signals in DMAS vs. N signals in DAS, which improves the signal-to-noise ratio (SNR);
3) the contrast resolution (which can be defined as the ability to detect targets with different echogenity also in the presence of acoustic clutter, due for example to side/grating lobes; usually it is associated to the pulse-

echo beamwidth at -40 dB or lower levels [27]) will be higher, as the side lobes will be lowered thanks to the multiplication stage (point 2) and to the auto-correlation window shaping.

B. Simulations and Experimental Setup

We compared the performance of F-DMAS to that of DAS on both simulated and experimental data, by evaluating the Point Spread Functions (PSF), beampatterns, synthetic phantom images and *in vivo* images.

Simulations were carried out in Matlab (The MathWorks, Natick, MA, USA) by using the Field II simulator [28], [29]. A linear array was modeled, which consisted of 192 elements with a pitch of 200 µm (element width = 170 µm, height = 3 mm, kerf = 30 µm) and a fixed elevation focus at 15 mm. A 32-element aperture was used in transmission and the focal depth was set to 15 mm. During transmission, the transducers generated a Gaussian-windowed 2-cycle sinusoidal burst at 12 MHz (68% fractional bandwidth at -6 dB). The array was supposed to perform 129 scan lines over the *xz* plane, covering a plane area ranging from x = -12.8 mm to +12.8 mm. A wider aperture (64 elements) was employed in reception.

The received RF signals were first BP pre-filtered. To exclude as much as possible the effects related to digital filters design, the BP filter was supposed to behave ideally in the rejected band; in the pass-band a Tukey window (α=0.5) was applied to the signal spectra, so as to limit the ripples in the time domain signals. The window frequency boundaries were empirically determined in order to well isolate all the signal band to be preserved; their values are resumed in Table I. Signal sampling frequency was 100 MHz.

Then beamforming with dynamic focusing was implemented. F# varied with depth as no dynamic apodization was applied (i.e. the active receive aperture width did not dynamically change), so that the different beamforming strategies could be compared using the same basic setup.

Also the BP filter applied after DMAS beamforming was simply implemented by applying a Tukey window (α=0.5) to the beamformed signal spectra. The window frequency boundaries (Table I) were again empirically determined by observing the spectral content of the simulated DMAS lines.

Experimental trials were carried out by employing the ULA-OP system [30]. Pre-beamforming RF data were recorded using the LA-435 12 MHz linear probe (Esaote, Genova, Italy), which consists of 192 piezoelectric elements with a 200 µm pitch, 3 mm height and a fixed elevation focus at 15 mm. The probe was driven by a Hanning-windowed 1-cycle sinusoidal burst at 10 MHz. A 32-element aperture was used during transmission and a 64-element aperture for reception. RF data were acquired while operating a 192-line B-mode scan and pre-filtered (Table I). The system sampling frequency was 50 MHz.

TABLE I
FREQUENCY BOUNDARIES OF THE BP-FILTER WINDOWS

	Pre-filter on RF signals	F-DMAS final filter
Simulation tests	4 – 18 MHz	6 – 30 MHz
Experimental test	5 – 15 MHz	8 – 24.99 MHz

An *in vivo* carotid artery image was obtained by setting the transmission focal depth at 15 mm, while dynamic focusing was implemented in reception. A Tukey window (α=0.5) was again used to implement the F-DMAS BP filter (Table I).

III. RESULTS

A. Simulated PSF and Beampattern at the Transmit Focus

In the first trials, the DAS and F-DMAS beamforming algorithms were tested and compared by simulating the scan of a single scattering point placed at the transmission focus in (x, z) = (0, 15) mm. To improve the PSF image detail resolution on the lateral direction, the density of scan lines was increased by shifting the active aperture by a shorter step (i.e. ¼ of the pitch).

The PSFs are represented in Fig. 2 over a 60 dB dynamic range (DR), and their axial and lateral profiles are shown in Fig. 3b-c. Besides, the amplitude spectra of the central beamformed lines and of the BP filter are shown in Fig. 3a.

The axial and lateral resolutions, measured as the main lobe width at -6 dB, are almost the same for DAS and F-DMAS, i.e. ~0.13 mm and ~0.2 mm respectively, as Fig. 3b-c show. However, for higher dynamic ranges, the main lobe of the two-way response is generally significantly narrower with F-DMAS (cf. Fig. 3c) and reaches a lower floor level compared to DAS (i.e., about -103 dB vs. -77 dB). Also the grating lobes at $x \approx \pm 10$ mm (which are due to relation between the array spatial sampling and the transmitted signal wavelength) are lower with F-DMAS (i.e., -66 dB vs. -52 dB).

These results clearly show that the contrast resolution is improved with F-DMAS. As said in Section II-A, this could be due mainly to two factors: i) the doubling of the central

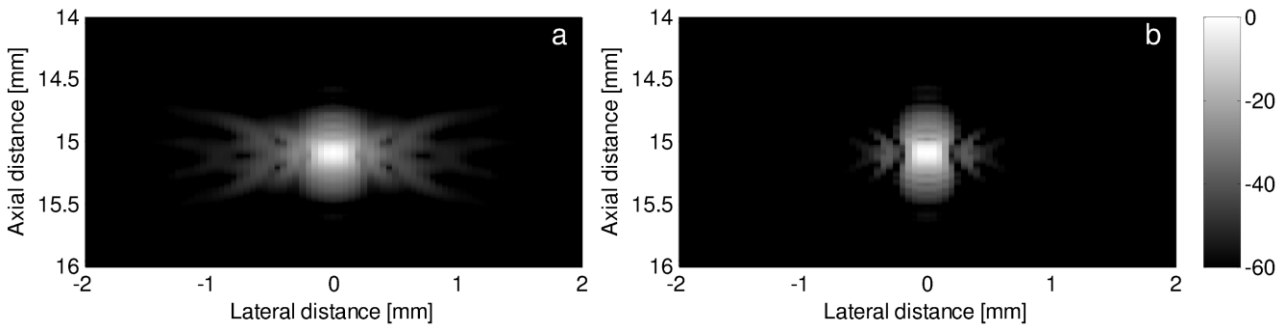

Fig. 2. PSFs at the transmission focal depth, obtained by employing a) DAS or b) F-DMAS. PSFs are shown over a 60 dB dynamic range (log-scale).

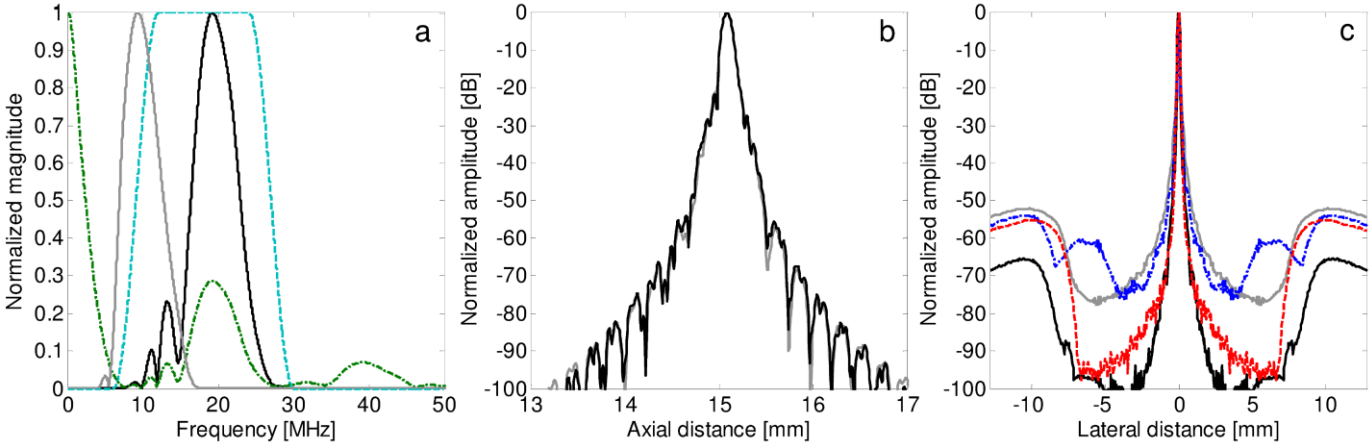

Fig. 3. a) The normalized amplitude spectrum of the central scan line (x=0 mm) of the PSF images in Fig. 2 is shown for DAS (gray line), F-DMAS (black line) and DMAS before BP filtering (dashed-dotted green line). The dashed cyan line represents the BP-filter window applied to the DMAS beamformed signals. b) Axial profiles of the PSFs at x=0 mm. c) Two-way normalized beampatterns at z=15 mm for DAS (gray line), F-DMAS (black line) and F-ABS (dashed-dotted blue line) with a 64-element receive aperture, and for DAS with a triangle-apodized 128-element receive aperture (dashed red line).

frequency of the F-DMAS beamformed signals and ii) the widening and triangle-shaping of the "artificial" aperture achieved by the aperture auto-correlation operation.

Hence, the following further analysis was carried out to separately study these two factors and to empirically demonstrate how they would impact on the lateral resolution. First, we tried to replicate the generation of the 2nd harmonic component in the beamformed signals, but without increasing the number of elements in the artificial aperture (i.e. the number of signals in the summation). This was achieved by implementing F-DMAS in the particular case in which s_i=s_j: in the practice, the absolute values of the N received signals were summed. We refer to this approach as F-ABS:

$$y_{F-ABS}(t) = \sum_{i=1}^{N} sign(s_i^2(t))\sqrt{\left|s_i^2(t)\right|} = \sum_{i=1}^{N} \left|s_i(t)\right|. \qquad (5)$$

Secondly, we considered the case in which DAS is applied to a receive aperture as wide as the one artificially achieved by the auto-correlation function, i.e. *2N-1* elements, with triangular apodization.

We then superimposed to the normalized two-way beampatterns obtained with DAS and F-DMAS in Fig. 3c also those obtained with F-ABS and DAS with a triangle-apodized 128-element receive aperture (*2N* elements were considered instead of *2N-1*, in order to keep symmetry).

The F-ABS beampattern shows a main lobe which is even narrower than that of F-DMAS, but the grating lobes are higher (-54 dB). Moreover, a new pair of grating lobes appear near to the main lobe (at $x \approx \pm 6$ mm), which are probably related to the doubled central frequency in reception. These two lobes can also be noticed in the F-DMAS beampattern but their level is very low (-97 dB with F-DMAS vs. -61 dB with F-ABS).

When applying DAS to a triangle-apodized 128-element aperture, the main-lobe width almost resembles that achieved by F-DMAS with 64-elements, as well as the adjacent side-lobe level. However, the grating lobes on the sides of the beampattern are still higher (-55 dB) than with F-DMAS.

These plots actually demonstrate that the narrowing of the F-DMAS main lobe is achieved thanks to both an increase in the central operating frequency of the imaging system and an artificial widening of the receive aperture. This last factor and the triangular apodization also contribute to the lowering of side lobes, which however is mainly achieved thanks to the spatial cross-correlation operation, as, on the whole, the F-DMAS beampattern shows the lowest side/grating-lobe level.

B. Simulated PSFs at Different Depths

Further analyses were carried out comparing DAS and F-DMAS in a scenario with several point-scatterers, placed side-by-side at different depths (from 5 to 50 mm with a 5 mm step), along the x=-3 mm, x=0 mm and x=+3 mm axial directions. The scatterers on the x=0 axis had an amplitude of 1; the amplitude of those on the left (x<0) was 0.25 while the amplitude of those on the right (x>0) was 0.5. The case in which white Gaussian noise is added to the received RF signals (prior to the pre-filtering stage) was considered too. The noise amplitude was set to be about 20 dB lower than the maximum RF signal peak, corresponding to the strongest reflecting point in the image.

In Fig. 4, the PSFs obtained by employing DAS and F-DMAS, also in the presence of noise, are represented.

From a quantitative point of view, the relative amplitude of the scatterers in the three lines (from left to right: -12 dB, 0 dB and -6 dB) is correctly represented also in the F-DMAS image, even at higher depths (z=50 mm), as shown by the PSF lateral profiles in Fig. 5. By using F-DMAS in the ideal case (Fig. 4b), the PSFs are narrower compared to DAS (Fig. 4a) and show reduced side lobes around the point targets and grating lobes, which implies that the proposed beamformer allows to achieve better image contrast resolution.

Both the -6 dB lateral resolution and -6 dB axial resolution of the PSFs in Fig. 4a-b are very similar for DAS and F-DMAS. Nonetheless, for lower amplitude values, the main lobe obtained with F-DMAS is significantly narrower than with DAS (Table II). Moreover, the main-to-side-lobe amplitude ratio around the point targets is higher for F-DMAS, i.e. contrast resolution is improved.

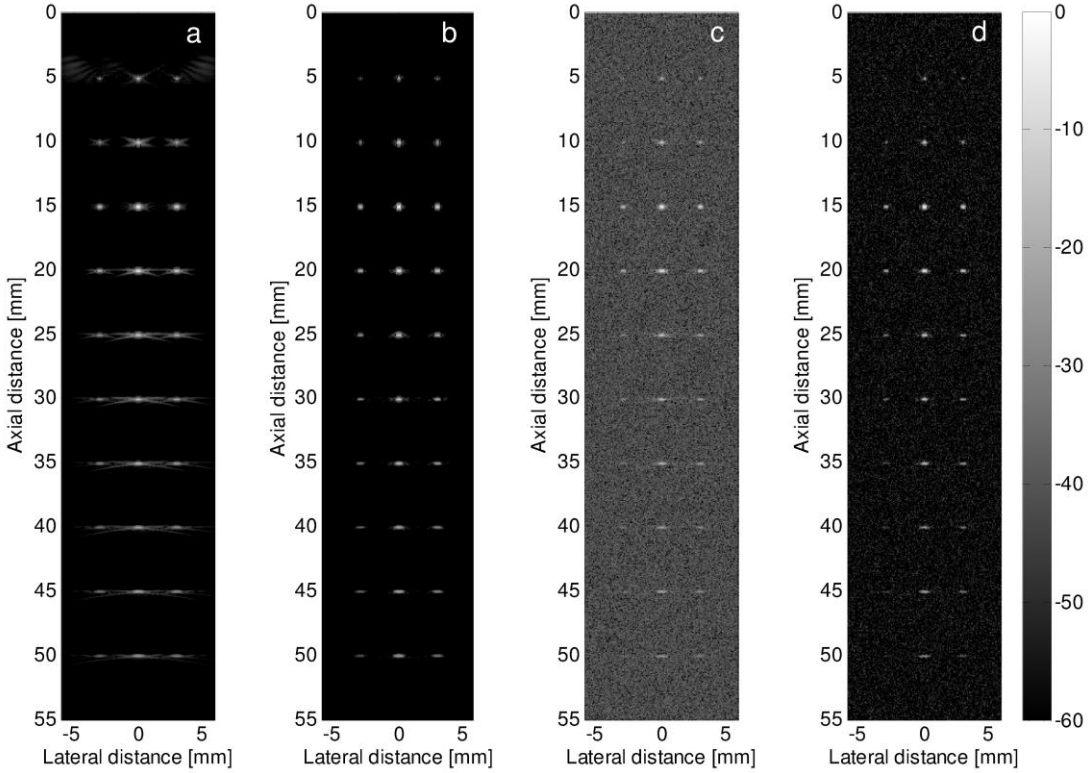

Fig. 4. PSFs obtained by employing DAS (a, c) or F-DMAS (b, d) beamforming, without (a, b) or with noise (c, d). Images are displayed over a 60 dB dynamic range (log-scale).

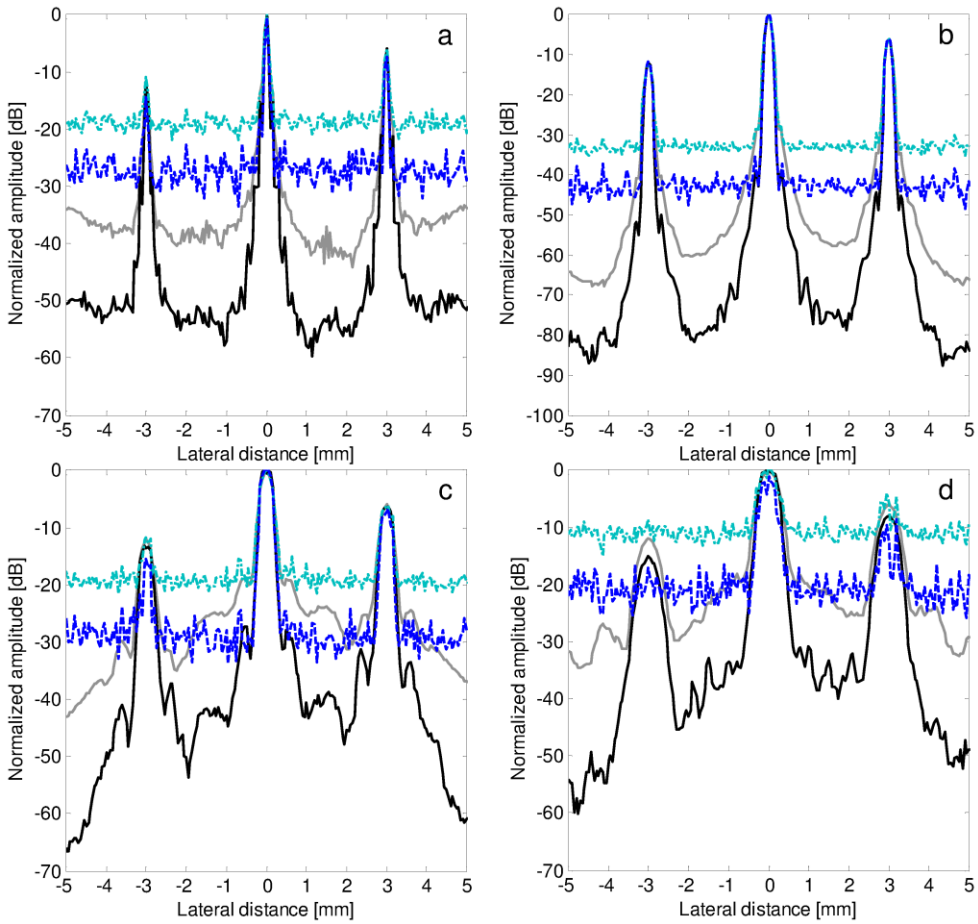

Fig. 5. Two-way normalized beampatterns at a) 5 mm, b) 15 mm (transmission focus), c) 30 mm and d) 50 mm depths, with DAS (gray line) or F-DMAS (black line) beamforming and without noise. The dashed-dotted cyan line and the dashed blue line refer respectively to DAS and F-DMAS when noise is considered.

However, it should be pointed out that nearer or farther from the aperture (e.g. at z=5-30-50 mm) the PSF peak values obtained with F-DMAS are 1-3 dB lower than with DAS.

Finally, Fig. 4c-d and 5 show that F-DMAS works correctly also when the SNR gets low, as it well suppresses the incoherent noise, which more significantly worsens the DAS image.

C. Simulated Phantom Image

Image formation capabilities and the obtained image quality were subsequently investigated by simulating the 2D scan of a synthetic phantom.

The test phantom consisted of 250000 points, randomly distributed in a 10x10x1 mm^3 volume (i.e. ~20 scatterers per resolution cell) centered at (x, y, z) = (0, 0, 15) mm. Inside this volume, the reflectivity had a Gaussian distribution [31].

A 3-mm-diameter cylindrical cyst was embedded in this region and centered at (x, y, z) = (0, 0, 15) mm. The cyst was supposed to be anechoic and the reflection coefficients of the scattering points inside it were set to zero.

Differently from the PSFs, the images in Fig. 6a-b have been represented over a 70 dB dynamic range, as we chose to highlight the fact that F-DMAS makes it possible to achieve an improved quality image even when displayed over a very high DR. Log-compressed images were finally also interpolated along the x axis.

It is immediate to notice that better defined cyst boundaries are achieved when employing F-DMAS beamforming (Fig. 6b) compared to DAS (Fig. 6a), thanks to the beam narrower main lobe and to the lower side lobes and noise floor. The mean gray level inside the cyst is also lower (Fig. 6c).

A quantitative measure of contrast can be given by the contrast ratio (CR) and contrast-to-noise ratio (CNR) [25]:

$$CR = 20\log_{10}\left(\frac{\mu_{cyst}}{\mu_{bck}}\right) \quad (6)$$

$$CNR = \frac{\left|\mu_{bck} - \mu_{cyst}\right|}{\sqrt{\sigma_{bck}^2 + \sigma_{cyst}^2}} \quad (7)$$

where μ_{cyst} and μ_{bck} are the mean image intensities (before log-compression) respectively in a small region inside the cyst or in the surrounding background (cf. Fig. 6), and σ^2_{cyst}, σ^2_{bck} are the corresponding variances. As expected, the contrast of the anechoic cyst is improved when applying F-DMAS: the CR is -60.9 dB while it is -44.4 dB with DAS. However the CNR is slightly lower with F-DMAS (1.3 vs. 1.8), as both the mean intensities and variance inside the cyst are lower, while the background speckle variance is about 1.4 times higher than with DAS.

TABLE II
LATERAL AND AXIAL RESOLUTION FOR THE PSFS IN FIG. 4a-b AT x=0 mm

		ML lateral width (mm)		ML axial width (mm)	
z (mm)	Level (dB)	DAS	F-DMAS	DAS	F-DMAS
5	-6	0.14	0.14	0.14	0.14
	-20	0.39	**0.33**	**0.34**	0.35
	-40	2.16	**0.83**	0.8	**0.65**
	-60	n.d.	n.d.	2.3	**1.02**
	-80	n.d.	n.d.	3.58	**2.7**
15	-6	0.21	**0.2**	0.13	0.13
	-20	0.38	**0.29**	0.25	**0.22**
	-40	0.97	**0.69**	**0.62**	0.63
	-60	n.d.	**1.41**	1.2	**0.95**
	-80	n.d.	n.d.	2.25	**1.84**
30	-6	0.39	**0.35**	**0.12**	0.13
	-20	1.33	**0.54**	**0.22**	0.25
	-40	n.d.	**1.7**	0.59	**0.55**
	-60	n.d.	n.d.	1.2	**0.98**
	-80	n.d.	n.d.	**2.1**	2.29
50	-6	0.65	**0.57**	0.11	0.11
	-20	1.92	**0.93**	0.26	0.26
	-40	n.d.	n.d.	0.64	**0.5**
	-60	n.d.	n.d.	1	**0.91**
	-80	n.d.	n.d.	2.23	**2.22**

The main lobe (ML) width is measured by considering the first cut-off of the beampatterns at the considered threshold level (dB); n.d. means "not defined". If small side lobes appear above the threshold, immediately adjacent to the main lobe, a measure of the total width of the main plus side lobe is provided. The best achieved values are highlighted in bold.

D. Experimental Results

Experimental trials were carried out in which *in vivo* carotid artery scans were performed. RF data were first pre- filtered and then beamformed to generate the images by employing both DAS and F-DMAS algorithms.

The images in Fig. 7 have been interpolated along the lateral direction and are represented over a 70 dB dynamic

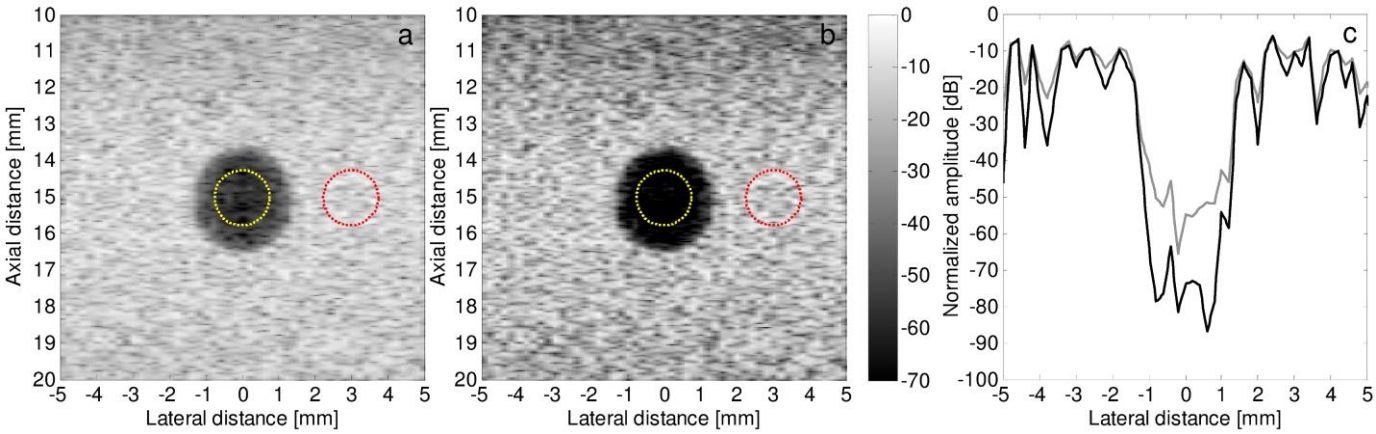

Fig. 6. Synthetic phantom images obtained with a) DAS and b) F-DMAS beamforming. Images are displayed over a 70 dB dynamic range (log-scale). The yellow and red dotted circles (same area) enclose the points which were used to compute respectively the cyst and background speckle statistics. In c) the lateral sections of the DAS (gray line) and F-DMAS (black line) images at z=15 mm are plotted.

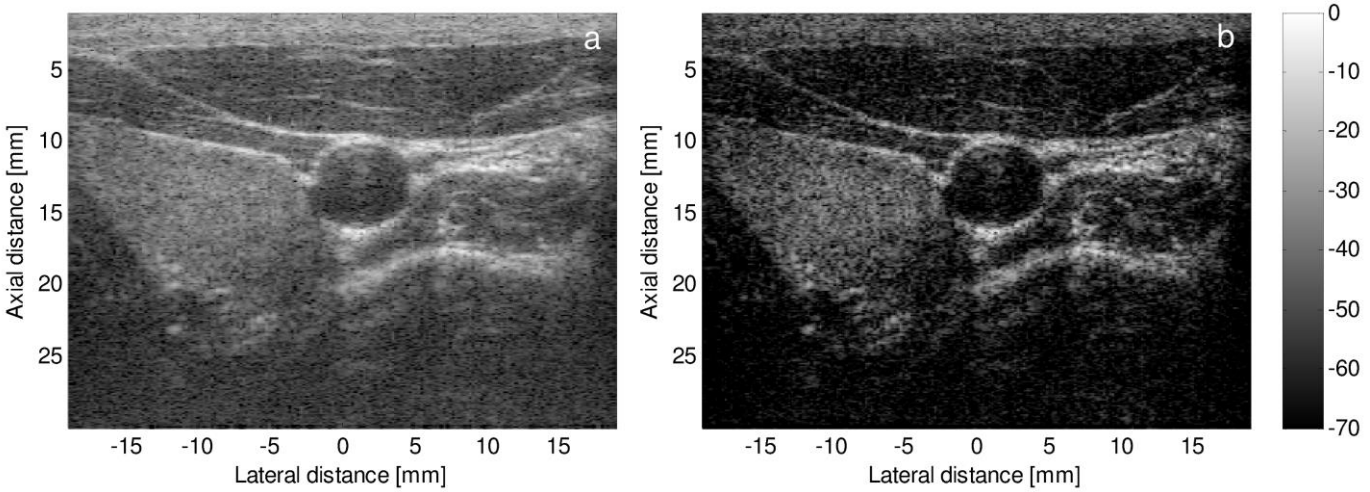

Fig. 7. B-mode *in vivo* images of the carotid artery, obtained with a) DAS and b) F-DMAS beamforming. Images are displayed over a 70 dB dynamic range (log-scale).

range. Also in this case, the F-DMAS gray-level image pixel distribution has a lower mean and higher variance than DAS, as the histograms in Fig. 8 show.

The quality of Fig. 7b is definitely improved: the contrast is higher than in Fig. 7a and the anatomical structures of interest are better highlighted, while the background noise floor is lowered. The lateral resolution is also higher, compared to the DAS image, and thus the carotid artery walls are better defined and the lumen is more clearly visible.

IV. Discussion

The main improvement introduced by the proposed beamforming algorithm is the significantly better contrast resolution, rather than detail resolution, if compared to DAS: images are better defined and the dynamic range for image visualization is higher.

With F-DMAS, in fact, the beam main lobe is narrower and side lobes are lower thanks to several factors. Firstly, the combinatory coupling, multiplication and sum of the backscattered echoes is equivalent to the computation of the non-normalized spatial auto-correlation function of the receive aperture; this means that an equivalent wider triangle-apodized aperture is achieved. Secondly, a band-pass filtering stage is used to isolate the echo signal frequency components centered around two times the fundamental frequency. Both these factors lead to an increased lateral resolution.

Furthermore, improved clutter suppression is achieved, as the F-DMAS algorithm brings a measure of the backscattered signal coherence into the B-mode image generation chain. The spatial cross-correlation of the received signals is indeed the starting point from which the signals to be used in the beamforming process are derived, by applying the square root and band-pass filter, so that the image lines have the desired dimensionality and frequency content. As these new "equivalent RF-signals" reflect the correlation of the backscattered echoes, the resulting PSFs show a narrow peak in correspondence of the target point and a lower noise floor and side lobes in the other directions.

However, a drawback of this method is that, if a single fixed transmission focal depth is used, the PSF amplitudes away from the focus are attenuated, as well as image intensity, since the maximum signal coherence occurs only in the transmission focal point. This amplitude loss is also slightly due to the final BP filtering stage, as can be noticed by changing the filter bandwidth. Anyhow, such a small inaccuracy could be easily compensated for by using the Time Gain Compensation (TGC) unit in the main system, which is manually adjusted by the operator based on a visual feedback. This operation would be in any case performed by the clinician to compensate for the fixed transmission focus.

The F-DMAS beamformer demonstrated to work correctly (i.e., preserving the relative amplitude of the scatterers in the final image) also in the presence of closely laterally spaced targets, placed at high depths (relative to the operating frequency). Even when the SNR got low, F-DMAS achieved a better rejection of the uncorrelated noise.

The phantom images obtained with F-DMAS show a higher

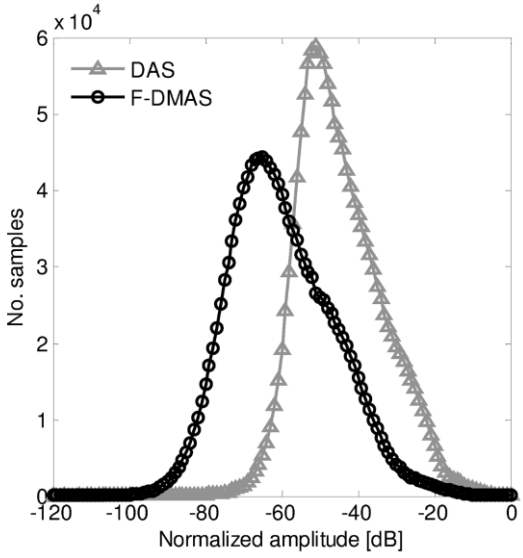

Fig. 8. Pixel intensity distributions for the DAS and F-DMAS images of the carotid artery, showing different mean and variance.

CR due to a significant reduction of the side-lobe level and narrowing of the main-lobe width compared to DAS. For these same reasons the phantom cyst shows an improved border definition, as well as the carotid artery lumen does.

However, with F-DMAS the CNR is limited by the increased speckle variance, which turns out into an alteration of the speckle pattern, as many more dark points appear in the image. A similar effect has been observed also in other works on adaptive beamforming [11], [32]. Some possible approaches to be considered in order to compensate for this alteration could be spatial compounding or time averaging, and this will be subject of future in-depth investigations.

The new algorithm performance has been confirmed by tests on a linear array for small-parts and vascular ultrasound imaging, as resolution and contrast are very important requirements for such B-mode imaging applications. Anyhow F-DMAS is expected to work well also with phased arrays, as the performance of this algorithm improve with the number of received signals, i.e. the number of signals summed together after pair combinations and multiplications. In phased arrays in fact, all the transducers can be used together to scan the desired volume/plane, differently from linear scans in which only a small aperture is used each time to transmit and receive the US beam. Thus, the number of received signals to be summed is generally higher, as well as the SNR of the final beamformed output, which would lead to an even better image quality. Besides, we should also consider that usually, in applications in which phased (or micro-convex) arrays are used, the system is set to work at high f-numbers and thus lateral resolution is limited, so further benefits could be brought about by the F-DMAS beamformer.

Some final remarks on computational times should be also provided. As initially pointed out, the DMAS algorithm involves a higher number of more complex operations, compared to DAS. Hence, the better performance of this algorithm come at the expense of an increased computational load and longer times, which could be a concern for real-time implementations, especially for 2D phased arrays where the number of active elements in the aperture is drastically higher.

Just to provide some quantitative data, we may suppose to implement the algorithm on a FPGA device, e.g. on an Altera FPGA of the Stratix IV family (Altera Corp., San Jose, CA, USA). If using the available library megafunctions to implement the floating-point multiplication and square root operations on double-precision operands, a latency of 5 and 57 clock cycles is required to generate respectively the multiplication and square root outputs, whit a maximum achievable frequency of 255 MHz and 366 MHz respectively, as reported in the floating-point megafunctions datasheet [33]. Consequently, (in the best case) F-DMAS will require at least approximately 62 clock cycles more than DAS to generate each signal which enters into the summation stage.

The algorithm also operates on a significantly higher number of signals, as RF signals are combinatorially coupled. Both an accurate resources utilization and timing analyses should thus be performed prior to a possible final hardware implementation.

Anyway F-DMAS could also be suitable for other ultrasound imaging application where real-time constraints are not fundamental (non-destructive tests, quality controls, etc.).

All in all, the proposed algorithm provides a good trade-off between the improvement of image quality (i.e., a higher contrast resolution) and the increase of computational load.

V. Conclusion

In this paper we demonstrate that the DMAS beamforming algorithm, originally conceived for RADAR imaging for breast cancer detection, is successfully modified and employed for ultrasound B-mode image formation.

Results of both simulated and experimental linear B-mode scans show that an increased contrast resolution, higher dynamic range and, consequently, better quality of the obtained images is achieved when using the improved DMAS (called F-DMAS) compared to standard DAS. This technique could be very promising for those applications which suffer from limited image contrast and resolution.

Future developments of this work are foreseen, which will include an analysis of F-DMAS operation in synthetic aperture imaging, in plane-wave imaging, and the implementation of spatial compounding methods which could possibly compensate for alterations in speckle texture.

Acknowledgment

The Authors thank the MSDLab group of the University of Florence, Italy, for providing the ULA-OP system, and also Dr. A. Ramalli and Prof. F. Leporati for constructive discussion respectively on image quality assessment and on possible FPGA implementation.

References

[1] K. Ranganathan and W. F. Walker, “A novel beamformer design method for medical ultrasound. Part I: Theory,” in IEEE Trans. Ultrason., Ferroelectr., Freq. Control, vol. 50, no. 1, pp. 15–24, 2003.

[2] K. E. Thomenius, “Evolution of ultrasound beamformers,” in Proc. IEEE Int. Ultrasonics Symp., San Antonio, TX, USA, 1996, pp. 1615–1622.

[3] K. E. Thomenius, “Recent trends in beamformation in medical ultrasound”. Available: http://folk.ntnu.no/htorp/Undervisning/MEDT8007/notater/TrendsBeamforming.Thomenius.pdf [Accessed: June 2013]

[4] M. Karaman, P.-C. Li, and M. O’Donnell, “Synthetic aperture imaging for small scale systems,” in IEEE Trans. Ultrason., Ferroelect. Freq. Control, vol. 42, no. 3, pp. 429–442, 1995.

[5] B. Van Veen, K. M. Buckley, “Beamforming techniques for spatial filtering,” in Wireless, Networking, Radar, Sensor Array Processing, and Nonlinear Signal Processing, CRC Press LLC, 1999.

[6] Z. Wang, J. Li, R. Wu, “Time-delay- and time-reversal-based robust capon beamformers for ultrasound imaging,” in IEEE Trans. Med. Imag., vol. 24, no. 10, pp. 1308-1322, 2005.

[7] J. F. Synnevåg, A. Austeng, and S. Holm, “Adaptive beamforming applied to medical ultrasound imaging,” in IEEE Trans. Ultrason., Ferroelectr., Freq. Control, vol. 54, no. 8, pp. 1606-1613, 2007.

[8] J. F. Synnevåg, A. Austeng, S. Holm, “A low-complexity data-dependent beamformer,” in IEEE Trans. Ultrason., Ferroelectr., Freq. Control, vol. 57, no. 2, pp. 281-289, 2010.

[9] M. Sasso, C. Cohen-Bacrie, “Medical ultrasound imaging using the fully adaptive beamformer,” in Proc. IEEE Int. Conf. Acoust. Speech Signal Processing, Philadelphia, PA, USA, 2005, pp. 489–492.

[10] K. Kim, S. Park, Y. T. Kim, S. C. Park, J. Kang, J. H. Kim, M. Bae, “Flexible minimum variance weights estimation using principal

components analysis," in Proc. IEEE Int. Ultrasonics Symp., Dresden, Germany, 2012, pp. 1275-1278.

[11] F. Vignon, M. R. Burcher, "Capon beamforming in medical ultrasound imaging with focused beams," in IEEE Trans. Ultrason., Ferroelectr. Freq. Control, vol. 55, no. 3, pp. 619–628, 2008.

[12] C. H. Seo, J. T. Yen, "Sidelobe suppression in ultrasound imaging using dual apodization with cross-correlation," in IEEE Trans. Ultrason. Ferroelectr. Freq. Control, vol. 55, no. 10, pp. 2198-2210, 2008.

[13] B. M. Asl, A. Mahloojifar, "Minimum variance beamforming combined with adaptive coherence weighting applied to medical ultrasound imaging," in IEEE Trans. Ultrason., Ferroelectr., Freq. Control, vol. 56, no. 9, pp. 1923–1931, 2009.

[14] J. A. Mann, W. F. Walker, "A constrained adaptive beamformer for medical ultrasound: initial results," in Proc. IEEE Int. Ultrasonics Symp., Munich, Germany, 2002, pp. 1807-1810.

[15] D. A. Guenther, W. F. Walker, "Robust FIR beamforming applied to medical ultrasound," in IEEE Trans. Ultrason., Ferroelectr., Freq. Control, vol. 56, no. 6, pp. 1168–1188, 2009.

[16] H. B. Lim, N. T. Nhung, E. P. Li, N. D. Thang, "Confocal microwave imaging for breast cancer detection: Delay-Multiply-and-Sum image reconstruction algorithm," in IEEE Trans. Biomed. Eng., vol. 55, no. 6, pp. 1697-1704, 2008.

[17] L. Wang, G. Jing, Z. Li, H. Xu, "A nonlinear adaptive beamforming algorithm based on least squares support vector regression," in Sensors, vol. 12, no. 9, pp. 12424-12436, 2012.

[18] T. Lo, H. Leung, J. Litva, "Nonlinear beamforming," in Electronics Letters, vol. 27, no. 4, pp. 350-352, 1991.

[19] S. Chen, L. Hanzo, A. Wolfgang, "Kernel-based nonlinear beamforming construction using orthogonal forward selection with the Fisher ratio class separability measure," in IEEE Signal Process. Lett., vol. 11, no. 5, pp. 478-481, 2004.

[20] E. D. Di Claudio, R. Parisi, G. Orlandi, "Application of the block recursive least squares algorithm to adaptive neural beamforming," in Proc. IEEE Workshop on Neural Networks for Signal Processing, Amelia Island, FL, USA, 1997, pp. 560-567.

[21] A. Trucco, V. Murino, "On nonlinear effects of envelope detection in beamforming systems," in IEEE Trans. Ultrason., Ferroelectr., Freq. Control, vol. 44, no. 4, pp. 948-952, 1997.

[22] S. T. Birchfield, "A unifying framework for acoustic localization," in Proc. European Signal Processing Conference (EUSIPCO), Vienna, Austria, 2004.

[23] V. Murino, C. S. Regazzoni, A. Trucco, G. Vernazza, "A non-coherent correlation technique and focused beamforming for ultrasonic underwater imaging: a comparative analysis," in IEEE Trans. Ultrason., Ferroelectr., Freq. Control, vol. 41, no. 5, pp. 621-630, 1994.

[24] R. Mallart, M. Fink, "Adaptive focusing in scattering media through sound-speed inhomogeneities: the van Cittert Zernike approach and focusing criterion," in J. Acoust. Soc. Am., vol. 96, no. 6, pp. 3721–3732, 1994.

[25] M. A. Lediju, G. E. Trahey, B. C. Byram, J. J. Dahl, "Short-Lag Spatial Coherence of backscattered echoes: imaging characteristics," in IEEE Trans. Ultrason., Ferroelectr., Freq. Control, vol. 58, no. 7, pp. 1377-1388, 2011.

[26] J. J. Dahl, D. Hyun, M. Lediju, G. E. Trahey, "Lesion detectability in diagnostic ultrasound with Short-Lag Spatial Coherence imaging," in Ultrason. Imaging, vol. 33, no. 2, pp. 119-133, 2011.

[27] T. L. Szabo, *Diagnostic Ultrasound Imaging: Inside Out*. New York, NY: Elsevier Academic Press, 2004.

[28] J. A. Jensen, "Field: A Program for Simulating Ultrasound Systems," in Med. Biol. Eng. Comput., vol. 34, pp. 351-353, 1996.

[29] J. A. Jensen, N. B. Svendsen, "Calculation of pressure fields from arbitrarily shaped, apodized, and excited ultrasound transducers," in IEEE Trans. Ultrason., Ferroelectr., Freq. Control., vol. 39, no. 2, pp. 262-267, 1992.

[30] P. Tortoli, L. Bassi, E. Boni, A. Dallai, F. Guidi, S. Ricci, "ULA-OP: an Advanced Open Platform for ULtrasound research," in IEEE Trans. Ultrason., Ferroelectr., Freq. Control., vol. 56, no. 10, pp. 2207-2216, 2009.

[31] J. A. Jensen, P. Munk, "Computer phantoms for simulating ultrasound B-mode and CFM images," in Acoust. Imag., vol. 23, pp. 75-80, 1997.

[32] J. F. Synnevåg, C. C. Nilsen, S. Holm, "Speckle statistics in adaptive beamforming," in Proc. IEEE Int. Ultrasonics Symp., New York, NY, USA, 2007, pp. 1545-1548.

[33] Altera Floating-Point Megafunctions User Guide. Available: http://www.altera.com/literature/ug/ug_altfp_mfug.pdf [Accessed: February 2014]